

Supplementary Data:

Engineering Cortical Neuron Polarity with Nanomagnets on a Chip

Authors:

Anja Kunze^{*,†,‡}, Peter Tseng^{†,‡}, Chanya Godzich[†], Coleman Murray^{†,‡}, Anna Caputo[§], Felix E. Schweizer[§] and Dino Di Carlo^{†,‡}

[†]Department of Bioengineering, University of California, Los Angeles, California 90095, United States

[‡]California NanoSystems Institute, University of California, Los Angeles, California 90095, United States

[§]Department of Neurobiology, University of California, Los Angeles, California 90095, United States

*corresponding author

Here, additional data and details are presented concerning the following parts of the article:

1. Methods.	2
2. Chip Design and Force Methodology.	7
3. Nanoparticle Uptake in Primary Cortical Neurons.	11
4. Single Cell Evaluation and Statistical Data Distribution.	13
5. Force Sensitivity within Cell Population.	16
6. Additional Video Files.	18
7. References.	18

1. Methods.

Fabrication of the Neuromagnetic Chip.

Fabrication of the neuromagnetic chip (Figure S1) is based on the micromagnetic chip published in Tseng *et al.*¹⁰ with modifications in the photoresist composition, patterning technique and chip design. Brief, Fisher glass slides were cleaned with Piranha (4:1) over night, rinsed with water and plasma cleaned (air, 100 °C, 200 W, 2 min). Glass slides were metalized sequentially with 30 nm titanium (Ti), 200–250 nm copper (Cu) and 30 nm Ti layers. The last Ti layer was microstructured using photolithography (KMPR, 7 – 8 µm height) and metal wet etching in 1% HF bath for 15 – 30 s. Subsequently, NiFe (80:20) alloys were electroplated in a custom electroplater bath (250 g/l NiO₄x7H₂O, 5g/l FeSO₄x7H₂O, 25 g/l boric acid, 1 g/l saccharin, 1 g/l sodium lauryl sulfate, pH 3.0) for 2h at 1V reaching a height between 5.5 µm and 7 µm. KMPR photoresist was stripped for 30 min in Aleg-355 (75 °C) and Ti-Cu-Ti layers were wet-etched with 1% HF (15–30 s) and 5% acetic acid / 15% H₂O₂ in water (70–90 s). Samples were cleaned in ultrasound acetone bath for 3 min and passivated with SiN layer (PECVD, 150 nm, 300 °C). PSR-5 low-fluorescent,¹¹ biocompatible, negative photoresist (5.4 µm = 3000 rpm, 1000 rpm/s) was spin coated over the magnetic alloys to cover them with about 1 µm layer of photoresist (6–8 µm, Fig. S1a). Different to previous studies are pre- and post- exposure bake times, which were 5 min at 65 °C, 10 min at 95 °C and 1 min at 65 °C, 2 min at 95 °C with 45 s float exposure (48 mJ/cm²) and 12 min hardbake at 120 °C. For poly-L-lysine (PLL) patterning, 1 µm AZ5214 layer was spun on the PSR-5 resist, underbaked (40–50 s, 95 °C), photolithographically patterned and developed (AZ400K/water solution, 1:4). The opened PSR surface was O₂ plasma activated (38 W, 30 s, 500 mTorr) and AZ5214 was removed through a 100% acetone rinse.

Engineering Magnetic Field Gradients and Characterizing Resultant Magnetic Forces.

To scale force magnitudes to a compatible level, several experimental parameters were considered. Based on an average cortical neuron cell diameter of 16 µm, magnetic field gradients on the order of 10,000 T/m¹ and the soft mechanical properties of neurons,² four different magnetic element (ME) geometries were chosen: (i) 12 µm × 16 µm, (ii) 8 µm × 16 µm, (iii) 4 µm × 16 µm and (iv) 4 µm × 8 µm. The orientation of the magnetic direction within the MEs is chosen to follow the orientation of the magnetic field. An aspect ratio greater than one was set to achieve stable uni-directional magnetization direction within the MEs. We then varied the orientation angle of the MEs to achieve slight shift in the magnetic field gradient. In our figures the different orientations of MEs were encoded with (i) 0°, *L* = length; (ii) 45°, *R* = rotational and (iii) 90°, *V* = vertical. All ME geometries were designed with a minimum pitch between the MEs of 83 µm and 1 µm between the MEs and the cell pattern.

A magnetically charged particle within a magnetic flux density gradient, referred as magnetic gradient in the main text (∇B), experiences magnetic forces (*F*, eq. 1) due to its magnetic momentum (*m*).

$$F = \nabla(m \cdot B) \quad \text{eq. 1}$$

Superparamagnetic micro- and nanoparticles in high gradient magnetic fields often form clusters, where the exerted force sums up based on the number i of agglomerated particles with a particle volume (V_p). From equation 2 we derived our resulting force (F) where $M_{p,sat}$ is the particle magnetization under magnetic saturation, $\nabla H(x, y, z)$ the gradient of the magnetic field strength and μ_0 the vacuum permeability.³

$$F = \mu_0 \sum_{i=1}^n V_{p,i} M_{p,i,sat} \nabla H(x, y, z) \quad \text{eq. 2}$$

The different force strengths of our multi-sized and oriented MEs were characterized using fluorescently labeled 1 μm diameter superparamagnetic iron oxide beads (MP, Chemicell, screenMAG, 45.5% Fe content, lot: 0502/13). According to the manufacturer, the bead saturation magnetization (M_s) was determined to be 3.8 mT ($M_{s, bead}$). We extracted magnetic forces based on a balancing force act of the magnetic and stokes forces at the bead, which is moving in a biological medium (PBS, $\eta = 1 \cdot 10^{-3} \text{Pa s}$) within a magnetic gradient.⁴ Since the externally applied permanent magnet generates a magnetic field at the MEs greater than the magnetization of the beads, we assumed a linear relationship (eq. 2) between magnetic force (F), permeability (μ_0) and the magnetic field gradient ($\nabla H(x, y, z)$, Fig. S2).

Magnetic bead movement was monitored using fluorescent and phase contrast microscopy, with the magnet slightly shifted to open the optical pathway. We extracted bead velocities (v_{\parallel}) parallel to the PSR-5 surface on our neuromagnetic chip with a treated PSR-5 surface of 2% Pluronic F127. Using MTrack⁵ for ImageJ bead trajectories were measured from time series (11 fps) and velocities extracted. We assumed frictional movement as described by Schaeffer *et al.* using a Faxen's Law coefficient $\lambda_{Faxen} = 2.29$ (eq. 3)⁶ to calculate force along trajectory positions (Fig. S3).

$$F_{stoke} = -6 \lambda_{Faxen} \pi \eta r_{h,p} v_{\parallel} \quad \text{eq. 3}$$

Based on a possible exponential decay of the gradient field, and the linear relation between field and force (eq. 2), estimated forces were assumed to scale down exponentially with distance from the MEs (Fig. S3). Three prescribed analytical models from literature were fit to the experimentally derived data: (i) exponential fit (eq. 4),⁷ (ii) a power fit (eq. 5)^{8, 9} and (iii) a logarithmic fit (eq. 6,⁷ Fig. S3 c2). The models were then evaluated based on residual distribution and R values (Fig. S3 d1–d3).

$$F(x) = F_0 + F_{max}(0) \cdot e^{Rx} \quad \text{eq. 4}$$

$$F(x) = F_0 + F_{max}(0)x^p \quad \text{eq. 5}$$

$$\ln F(x) = f + Rx \quad \text{eq. 6}$$

Nanoparticle (NP) induced forces (F_{NP} , eq. 7) were estimated based on magnetic nanoparticle properties (m_{NP}) in relation to magnetic bead properties (m_{MP}) see eq. 8. Where r is the radius of the particles, core% the iron core percentage and δ the material density (data from manufacturer). Based on manufacturer data, purchased nanoparticles (Chemicell, fluid/nano-screen-MAG, 100 nm) contained 63% iron, with $M_{s,NP} = 41 \text{ mT}$ (Table S1). Finally different nanoparticle cluster formations were considered scaling F_{NP} up based on a spherical volume.

$$F_{NP} = F_{MP} \cdot \frac{m_{NP}}{m_{MP}} \quad \text{eq. 7}$$

$$\frac{m_{NP}}{m_{MP}} = \frac{\rho_{NP} \cdot V_{NP} \cdot M_{NP,sat}}{\rho_{MP} \cdot V_{MP} \cdot M_{MP,sat}} = \frac{M_{sat,NP} \cdot \rho_{NP} \cdot core\%_{NP} \cdot r_{NP}^3}{M_{sat,MP} \cdot \rho_{MP} \cdot core\%_{MP} \cdot r_{MP}^3} \quad \text{eq. 8}$$

Table S1: Particle parameter from manufacturer

Particle type	Commercial name	Core%	Density	Diameter	M _s
Micro particle	screenMAG	45.5	2.25 g/cm ³	1 μm	3.8 mT
Nano particle	nano-screenMAG/ fluidMAG	63	1.25 g/cm ³	100 nm	41.5 emu/g

Single Cell and Cell Population Pattern.

Single cell patterning was inspired by micropatterned ratchets.^{12, 13} Our ratchet design consisted of one square (15 μm × 15 μm, P0), where the neural cell body should adhere and arrow shaped ratchets (14.5 μm × 15 μm, P1) with one (P2) to five (P6) repetitions for directional neurite outgrowth (Fig. S9 b2). Cell population patterning was established on stripes of 20 μm, 50 μm, 100 μm, 150 μm, 200 μm and 300 μm widths; and 2 mm lengths. We used competitive co-adsorption¹⁴ of Pluronic F-127 and PLL to hydrophobic and hydrophilic photoresist surfaces. Hydrophilic photoresist areas were generated through O₂ plasma. Pluronic powder F-127 (Sigma-Aldrich) was dissolved in phosphate buffered saline (PBS) at 2 % (w/v) for stock and sterile filtered, final 0.05 (w/v) Pluronics, 25% (v/v) PLL in PBS solution was prepared as needed. After plasma activation of the PSR-5 surface, chips were UV sterilized for 20 min and covered with the Pluronic/PLL solution for subsequent 16 h at 37 °C. After, solution was aspirated and culture medium (Neurobasal, 10% horse serum) applied until cell seeding.

Neuronal Cell Culture.

For our cortical neuron culture, cortical hemispheres were dissected from whole rat brains (E18, BrainBits) and dissociated with 10 % (v/v) Papain (Carica papaya, Roche) in Hibernate®-E (BrainBits). In depth, whole rat brains were transferred to PBS (33mM glucose, 1% (v/v) Penicillin-Streptomycin (PenStrep from Gibco®)), washed for 5 min and dissected. Cortical tissues were placed in Papain/Hibernate-E (pH 7.3) and dissociated for 15 min at 37 °C. Papain/Hibernate was replaced by 10% horse serum (Fisher Sci) in Neurobasal (Gibco®). Dissociated tissues were triturated through a 1000 μl pipette tip and filtered through a cell strainer (40 μm). For cell counting, neurons were centrifuged (6 min, 600 rpm, 4 °C) and re-suspended in Neurobasal (2 % (v/v) serum free B-27®, 1% (v/v) GlutaMAX™). Finally, cortical neurons were seeded on the neuromagnetic chip at final concentration of 500,000 cells/ml (gently, dropwise seeding of about 500 μl, if necessary repeated) and incubated (95 % air, 5 % CO₂, 65 % R.H., 37 °C). After 2 h, unattached cells were washed away with pre-warmed culture media.

Force Induced Cell Polarization and Migration.

To induce an intracellular mechanical force, cortical cells were exposed to a mixture of three types of functionalized-fluorescent super-paramagnetic nanoparticles (fMNP, Chemicell, 1:1:1 in Neurobasal, 1 % PenStrep, 1 % GlutaMAX™, 2% B-27, 10 μg/ml each): (1) glucuronic acid, (2) starch and (3) chitosan (Fig. S1). Control studies indicated (Fig. S2, and S3) different fMNP uptake location sites in neuron cultures, thus all three fMNPs were used simultaneously to prevent heterogeneous force distribution due to pathway selective uptake. At 1 day *in vitro* (DIV)

the adhered cortical neurons were exposed to fMNP suspension through medium replacement, which exposed one cell to approximately 36000 fMNPs, ~5 % of the cell volume. Cortical neurons were incubated for up to 6 h with the fMNP suspension and washed with pre-warmed media prior to applying a permanent magnetic. The cultures were exposed to three strengths of magnetic fields: 100 mT (½ in. x ½ in. x 1/8 in., Apex Magnets), 150 mT (½ in. x ½ in. x ½ in., Apex Magnets) and 480 mT (1 in. x 1 in. x 1 in., K&J Magnetics) rare earth magnets for up to 24 h.

Immuno Fluorescent Labeling.

For fluorescent and confocal microscopy, cortical neurons were washed with Dulbecco's phosphate-buffered saline (DPBS with magnesium and calcium, Gibco) and fixed for 20 min with paraformaldehyde (4 % (v/v) PFA/PBS, Santa Cruz Biotechnologies), permeabilized with 0.1% Triton-X/DPBS and 3 % BSA for 10 min, and blocked with 3 % goat serum in 1% BSA/DPBS. Primary antibodies were incubated overnight (4 C) in 3 % goat serum, 0.5 % Tween-20 in 1% BSA/DPBS and secondary antibodies for 2 h (room temperature). Finally 4',6-diamidino-2-phenylindole (DAPI, 300nM in DPBS,) was incubated for 15 min and additionally mounted on glass slides using pro ProLong® Gold antifade reagent (Molecular Probes). Based on literature, we assumed a correlation between microtubule formation and forces,¹⁵ thus we selected antibody staining specifically against microtubule associated proteins tau in axonal projections, and MAP2 in dendritic projections. Primary antibodies utilized included: rabbit anti-GFAP (1:200), chicken anti-MAP2 (1:200), mouse anti-TAU-5 (1:200) and Fluor488 anti-Tubulin-beta-III and secondary antibodies utilized included: DyLight 405 anti-rabbit IgG (1:500), CY-5 anti-mouse (1:300) and Alexa Fluo568 anti-chicken (1:500). Depending on the staining, the fMNP fluorescent unit was selected to be either green: ex. 476 nm, orange: ex. 524 or red ex.578.

Nanoparticle and Magnetic Field Characterization.

Due to reported changes in hydrodynamic radius of nanoparticles in culture medium,¹⁶ we determined zeta-potential and hydrodynamic radius using Zetasizer Nano (Malvern Instruments Ltd) for each individual charged fMNP in 2 %B-27, 1% GlutaMAX™, 1% PenStrep in Neurobasal at 37 °C. Additionally, fMNP fluorescence and cluster formation was monitored on control slides (Media, PSR-5, no cells). Field strengths of the rare earth magnets in x-, y-, z-directions were characterized using Gauss/Teslameter (Series 9960, F.W. Bell, transverse Hall probe) above the magnet through a 1–1.2 mm glass slides at 5 mm pitched grid points.

Image Acquisition.

Live cell experiments were performed on-chip to evaluate neural cell position on stripes, before and after magnet application (24h later). These were imaged using wide-field fluorescent (fMNP) and phase contrast (PC) in a life cell incubator on top of an inverted fluorescent microscope (Nikon, 20x, 40x air objectives). Fluorescent labeled cortical neurons on cultured chips were captured using a semi-automated programmable XY stage (NIS-elements, DAPI, FITC, TRITC, CY-5 filter). Chips were consistently referenced for image capture with cell pattern position pointing towards right (positive-X-axis) and with ME position opposed, pointing towards left (negative-X-axis). Multichannel, z-stacked laser confocal fluorescent images were acquired using a Leica SP2 confocal microscope (63x, 100x, oil objective) with argon laser: ex. 488 nm (fMNP-FITC/green), 3 helium-neon lasers: ex. 594 nm (MAP-2, Tubulin-TRITC/red) and 633 nm (TAU-5-Far-red) and near UV laser: ex. 405 nm (DAPI-Blue). Bead displacement was imaged through 20x DIC air objective in PC (Nikon, inverted) at 60 fps.

Image Analysis.

Single cell polarization was quantified using 4-fluorescent channels and phase contrast stack images (12-bit) in ImageJ. For each neuron, we measured an orientation vector originating from the nucleus centroid to the centroid of neuronal tau staining (Fig. S7). Centroids were determined based on elliptical fit to the nuclei (DAPI-channel) and protein staining (CY5-channel) and used to extract cell body/nucleus area, perimeter, minor, major, angle, circularity and skew. Uptaken fMNPs (FITC-channel) were quantified through particle counting, when colocalized with TAU-5, MAP2 or Tubulin staining. MAP-2 staining (TRITC-channel) and morphological appearance in phase contrast were used to confirm the location of cell bodies and MEs. Data reproducibility was monitored using the region of interest manager (ROI manager in ImageJ). The location of a single neuron was reported based on its triangle or square position, which also reports the proximity to MEs, where six equals farthest (6th triangle) and one equals closest (square). Further, we documented geometry of pattern (P1 – P6), uptaken fMNPs based on the following particle cluster area (A_{cluster}) code (class 0: no fMNP, class I: few nanoparticles, $A_{\text{cluster}} < 0.5 \mu\text{m}^2$, class II: few clusters, $A_{\text{cluster}}: 0.5 \mu\text{m}^2 - 1.0 \mu\text{m}^2$, class III: multiple dots, $A_{\text{cluster}}: 1.0 \mu\text{m}^2 - 2.0 \mu\text{m}^2$, class IV: all clusters, $A_{\text{cluster}} > 2.0 \mu\text{m}^2$) and orientation and type of ME (L, R, V, $4 \mu\text{m} \times 8 \mu\text{m}$ – $16 \mu\text{m} \times 12 \mu\text{m}$). Cell population behavior was analyzed based on normalized fluorescent signal plots. ImageJ surface intensity values (I) were extracted over constant regions of interest of PLL pattern widths by $20 \mu\text{m}$ pattern lengths. Multiple intensity plots were averaged for the same condition, and normalized to the minimum signal intensity (I_{min} : signal noise, background) with $I/I_{\text{min}} = 1$ for no signal.

Statistical Evaluation.

From the orientation vector, absolute vector length, x-projected vector length and orientation angle were extracted. Histogram plots for x-projected vector length shows length distribution in 13 length bins between $-6 \mu\text{m}$ and $6 \mu\text{m}$. Histogram plots for orientation angle shows angle distribution in 4 angle bins of 90° around 45° , 135° , 225° and 315° . Histogram plots were tested for normality using D'Agostino's K-squared test based on skewness, kurtosis and omnibus. As the location of protein distribution is restricted by the cell membrane and most neuronal proteins can be found somewhere in the soma, we expected a shift in median position rather than a significance in mean location or variance. Significance of tau protein orientation was tested using the non-parametric one-sample Wilcoxon signed rank test with null-hypothesis median ≥ 0 and $p < 0.05$ (OriginPro 9). Significance of tau protein polarization (how far maximum signal from tau protein was located from the nucleus center point) was tested on absolute vector length after normality test using either one-way ANOVA, $p < 0.05$ (no rejection of normality) or non-parametric Kruskal-Wallis ANOVA $p < 0.05$ (normality rejected). Normalized signal intensity plots I/I_{min} were normality tested and signal distributions compared based with Kolmogorov-Smirnov Test ($F(x) \neq G(x)$, $p < 0.001$) and Friedman ANOVA ($p < 0.005$).

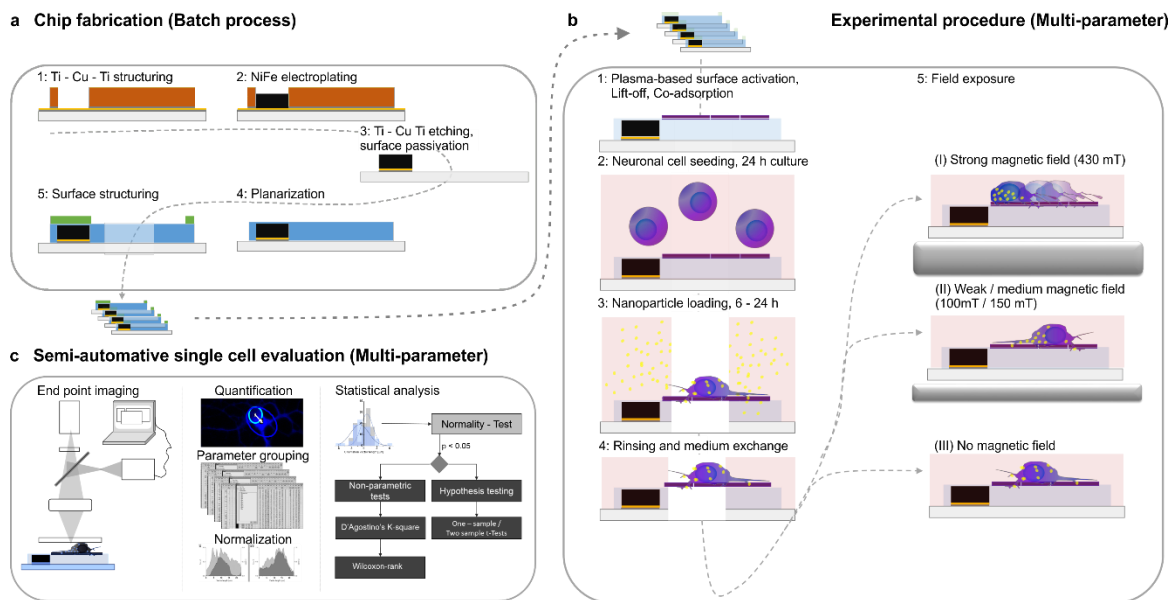


Figure S1: Experimental work flow consists of three parts (a) chip fabrication occurring in batch process, (b) experimental cell culture procedure with magnetic field exposure over 24 h. (c) Final off lab quantification and evaluation procedure.

2. Chip Design and Force Methodology.

The strength of the external magnetic field were chosen to magnetize the ferromagnetic NiFe magnetic elements (ME) and the functionalized superparamagnetic iron oxide nanoparticles (fMNPs). However, size and strength of the rare earth permanent magnet impacts the magnetic field gradient. The neuromagnetic chip design was initially adapted to small magnetic field magnets ($B_{\max} = 100 \text{ mT}$). Figure S2 shows the measured magnetic field of two attached permanent magnets underneath the neuromagnetic chip. Due to distinct characteristic length scales of the permanent magnet and the micrometer sized MEs, we can assume same field conditions for at least five cell arrays of 5×14 cell patterns.

The magnetic field gradient attracts the majority of magnetic beads or nanoparticles to one or more dominant trap points around the MEs. We experimentally estimated magnetic force attenuation at the most dominant trap point through velocity measurements of magnetic beads, shown in Figure S3. Force-distance relation can be estimated from power^{8, 9} or exponential fit.⁷ For our data set, a linear fit on logarithmic scaled data resulted in the best residual distribution.

Since the force gradient depends on the particle trajectory, we estimated for each ME size a unique maximal force amplitude, and an averaged gradient profile from consolidated data points (Figure S4). Table S2 gives the fit parameters and extracted force amplitude at $1 \mu\text{m}$ distance from ME as designed. All force estimations in our article are based on the extracted force amplitudes and were scaled by size, by nanoparticle content and by external magnetic field strength.

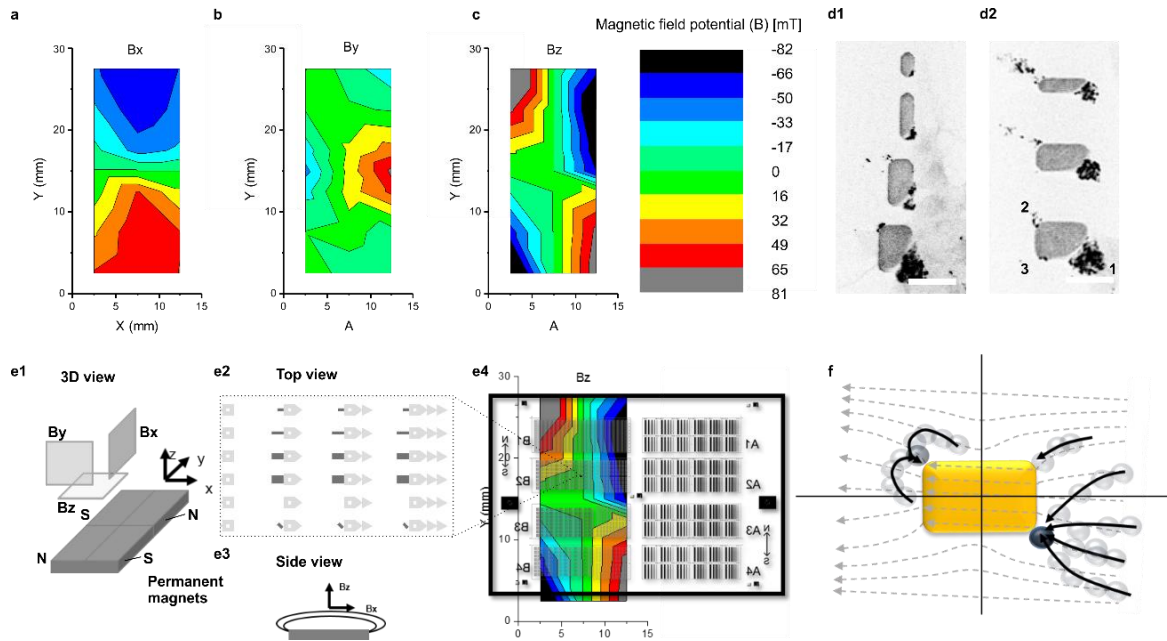


Figure S2: Magnetic elements act as a sink in a permanent magnetic field and generate magnetic field gradients. (a–c) Permanent magnetic field potentials were measured for two attached $\frac{1}{2} \times \frac{1}{2}$ in. weak magnets in x-, y-, z- planes with a Gaussmeter above a 2 mm glass slide. (d1, d2) Magnetic elements (ME) induce field gradients and trap points of superparamagnetic nanoparticles (fMNPs) at 1st, 2nd, and 3rd order trap points. ME size and orientation impacts the amount of trapped fMNPs. (e1) Magnetic field planes in 3D and schematic (e2) top and (e3) side view of ME design juxtaposed to cell adhesion patterns (gray arrows). (e4) Chip design placed over two permanent magnets with local differences of permanent magnetic field at the macro scale and constant field potential at the microscale. (f) ME design and dimensions induce 1st, 2nd and 3rd order micro- and nanomagnetic particle trap points.

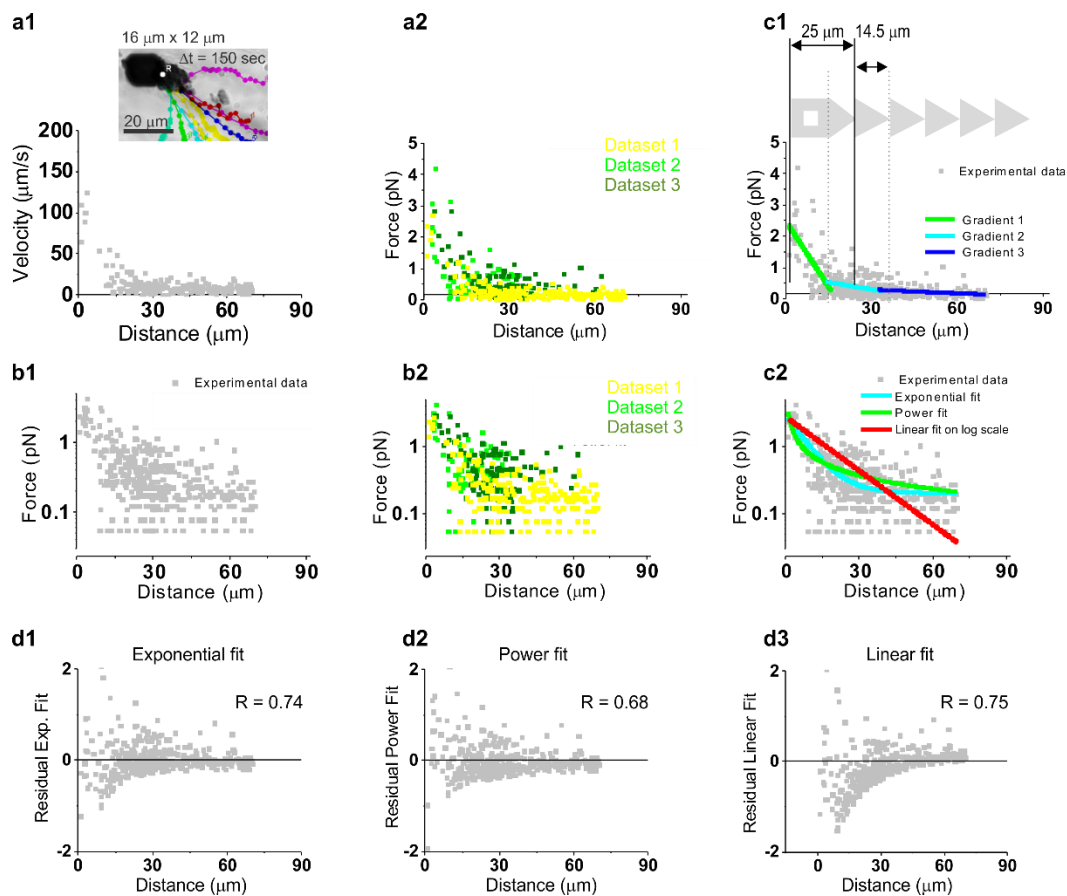


Figure S3: ME induced trap force quantification using time lapse videos of magnetic microbead motion. (a1) Velocity-distance scatter plots were extracted from video files for different sized magnetic elements ($n = 1$). (a2) Velocity plots were converted to force plots using Stokes' and Faxén's law ($n = 3$). (b1) Consolidated data scatter plot in logarithmic scale from (b2) multiple datasets was used to estimate force fit ($n = 3$). (c1) Linear force gradients can be extracted over specific pattern dimensions, however, magnetic gradient induced forces correlated best with a linear fit model in the logarithmic scale. (d1–d3) Residual distribution of different fit models with best symmetry and highest R value for linear fit model.

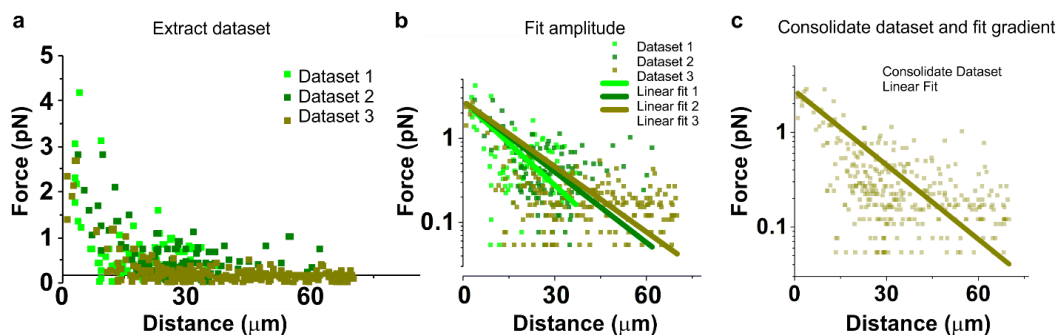


Figure S4: Parameter extraction for linear fit model of different sized magnetic elements. (a) Input data is the transferred force-distance scatter plot. (b) The location of the attracted micro- or nano particle and the ME within the permanent magnetic field impacts the force gradient; however, the trapping force should be determined *via* the size and was therefore fit for single data plots independently of the gradient. (c) Averaged gradients from same sized MEs were estimated in a 2nd step and were based on consolidated data plots keeping the maximum trap force constant.

Table S2 Linear fit parameters and empirical estimate of maximum trapping force (A_0) and force gradients in relation to magnetic element size and orientation within the field.

Magnetic Elements		Fit parameters			Goodness		Force estimate	
Dimension	Orientation	Averaged A_0 @ 1 μ m	Averaged gradient	SD gradient	R-value	n	Fmax @ 1 μ m	SD F
<i>low external field</i>								
12 x 16	Length (0)	0.44	-0.0260	0.0015	0.81	3	2.58	0.02
8 x 16	Length (0)	0.35	-0.0509	0.0022	0.81	3	1.98	0.05
4 x 16	Length (0)	0.15	-0.0322	0.0008	0.84	5	1.25	0.02
4 x 8	Length (0)	-0.10	-0.0076	0.0003	0.80	3	0.78	0.00
12 x 16	Rotation (45)	0.58	-0.0280	0.0008	0.80	4	3.52	0.11
8 x 16	Rotation (45)	0.40	-0.0260	0.0021	0.56	3	2.32	0.07
4 x 16	Rotation (45)	0.25	-0.0183	0.0012	0.44	3	1.71	0.03
4 x 8	Rotation (45)	0.10	-0.0228	0.0015	0.83	1	1.19	--
12 x 16	Vertical (90)	0.70	-0.0394	0.0022	0.73	3	4.55	0.32
8 x 16	Vertical (90)	--	--	--	--	--	--	--
4 x 16	Vertical (90)	0.28	-0.0388	0.0028	0.79	2	1.74	0.01
4 x 8	Vertical (90)	0.40	-0.0308	0.0007	0.78	3	2.33	0.02
<i>medium external field</i>								
12 x 16	Length (0)	0.60	-0.01181	0.00025	0.23	3	3.88	0.03
8 x 16	Length (0)	0.45	-0.01040	0.00026	0.26	2	2.74	0.03
4 x 16	Length (0)	0.20	-0.00210	0.00044	0.45	1	1.58	--
4 x 8	Length (0)	0.05	-0.00190	0.00051	--	1	1.12	--

Legend:

n = number of data sets; F = magnetic force; SD = standard deviation

3. Nanoparticle Uptake in Primary Cortical Neurons.

In contrast to other cell types, little information about fMNP uptake in cortical neurons could be retrieved from literature.^{16, 17} However, we assumed that in cortical neurons different functional groups would alter nanoparticle uptake in neurons and astrocytes, and determine their localization after 6 h uptake.¹⁸ In cell culture control studies we examined the cellular uptake by neurons and astrocytes and a general astrogliosis (GFAP immunostaining) of originally negatively charged (glucuronic acid-ARA and Starch) and positively charged (Chitosan) fMNPs (Table S3, Figure S5). In summary, 6 hr fMNP uptake seemed to be sufficient to see a green fluorescent signal (from fMNPs) co-localized with neural cell makers (MAP2, TAU-5) and still obtain a negative GFAP signal (no astrogliosis). The surface functional group seems to determine the localization where nanoparticles interact with neurons, how fast neurons take the fMNPs up, and whether they cause toxicity. Glucuronic acid nanoparticles co-localize with MAP-2 (Figure S5 c1). Starch nanoparticles accumulate and cluster at the end of neurites and in the soma (Figure S5 c2). In the soma there might be endosomal release based on observation of a diffuse green signal. Chitosan nanoparticles adhere between cells and along neurites, however, after more than 6 h exposure to nanoparticles cells show signs of reduced neurite outgrowth and nanoparticle spots along neurite filaments (Figure S5 c3). These preliminary study led to our final decision to use all three functionalization schemes of the fMNPs at the same time in a 1:1:1 ratio. Thus, neurons are getting exposed to the same amount of iron oxide content with fMNPs spread over the whole cell.

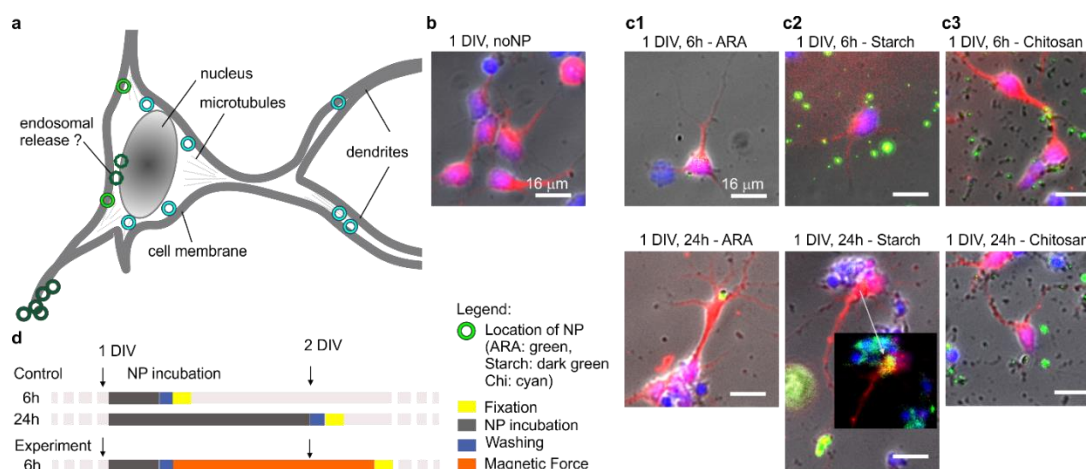


Figure S5: Localization of nanoparticle uptake is determined through the functional group of the iron oxide particles. (a) Schematic of neural cell with different nanoparticle uptake localizations, summarized from control studies. (b) Neurons on glass surface stained against microtubules associated protein (MAP2, red) and cell nucleus (DAPI, blue). (c) Nanoparticle uptake into cortical neurons after 6 h and 24 h loaded to media at 1 day *in Vitro* (DIV) with functional surface modification as indicated: (c1) glucuronic acid, (c2) starch and (c3) chitosan.

Up-taken clusters of fMNPs were evaluated in our study using wide-field fluorescent microscopy, which made it challenging to visualize small amounts of particles taken up(Figure S6).

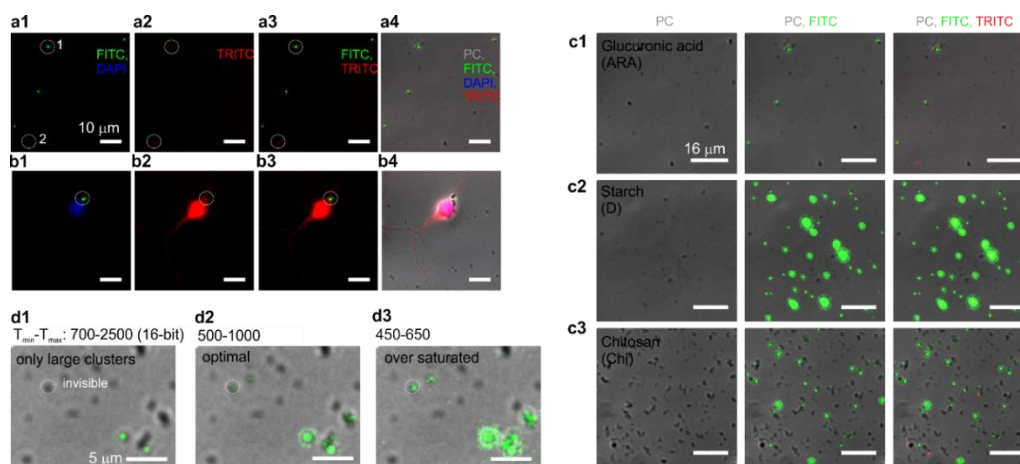


Figure S6: Fluorescent images show fluorescent signals from fMNPs and their relation to unspecific binding and cellular compartments. (a and b) FMNPs on a glass surface emit bright fluorescent signal in the FITC channel (a) outside and (b) inside cells. (a1) Fluorescent signal from fMNPs in FITC without cells. (a2) FMNPs may emit a very weak fluorescent signal into the TRITC channel, grey circle #1. (a3) Circle #2 points out nonspecific binding in TRITC channel not from fMNPs. (a4) In phase contrast, nanoparticles are visible as black dots, however, black dots may also be debris (see b4). (b1) Nanoparticles can be detected adjacent to cell nuclei (b2) Red dot signal indicates co-localization of nanoparticle within the cell body surrounded by MAP-2. (b3) Green fluorescent signal confirms that the red dot is a nanoparticle, now fluorescently visible in the FITC channel. (b4) Phase contrast with overlaid fluorescent image. Thus fMNPs are best identified through (a4) co-localization of phase contrast and fluorescent signal and can be considered attached or up-taken by neurons when (b1) visually next to a DAPI (cell nucleus) staining and co-localized with a cytoskeleton staining like (b2–4) MAP2 (red), tau or tubulin. (c) Different surface coating on fMNPs impact nanoparticle dispersion in media, surface adhesion and fluorescent signal brightness. (c1) Glucuronic acid coated nanoparticles show low cluster formation. (c2) Starch coated nanoparticles show high cross fluorescence into the TRITC channel and large cluster formation. (c3) Chitosan show high stickiness, but low cross fluorescence. Used threshold gray image settings: 500–1000 (16-bit) (d) FMNP signal strength depends on cluster size. (d1) Signal depth threshold is optimal for larger nanoparticle clusters, however, fluorescent signal from smaller nanoparticle clusters remains undetected. (b2) With standard fluorescent microscopy fluorescent signal from fMNPs can be detected through (d2–3) signal oversaturation by choosing the optimal exposure time and signal depth settings.

Table S3: Nanoparticle characterization based on physical and handling properties.

Shell, functional group	Hydrodynamic radius [nm]*	Z-Potential [mV]*	Cluster	Stickiness	Fluorescence	Cross fluorescence	Uptake
ARA, carboxyl group	110	-8.8	low	low	low	moderate	low
Starch, hydroxyl group	280	15.3	high	high	high	high	moderate
Chitosan, amino group	275	-9.5	moderate	high	high	low	high
Ideal			low	low	high	low	high

Legend:

Color code

hindered ideal ok

* measured in Neurobasal with B27 @ 37°C

4. Single Cell Evaluation and Statistical Data Distribution.

General increase of axonal outgrowth in correlation to the addition of fMNPs is often reported for 48 h and above, and can be visualized in an unsigned vector length plot. In our case, however, the extracted values are restricted to the somata and very young cortical neurons (< 48 h) as we were interested in engineering the intracellular tau distribution early during development and before the first signs of neuronal polarization (defined axonal outgrowth and dendrite establishment) take place (thus before stage 3). The on-chip parallelized force mediation yielded a diverse range of cell parameters. Intracellular tau distribution in neural cells was easiest to quantify based on TAU-5 staining and extracting an orientation vector. Figure S7 shows how tau gets distributed in neurons after their stage 2 and how our derived orientation vector correlates with the direction of axonal outgrowth in stage 3 neurons (5 days *in vitro*).

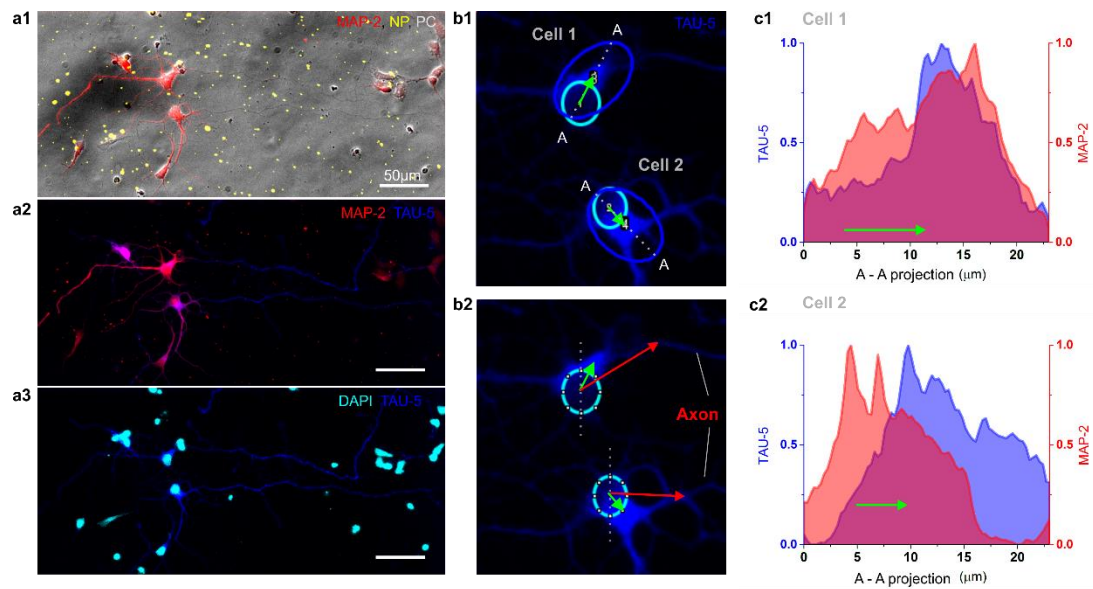


Figure S7: Characterizing immunofluorescent staining of TAU-5 and MAP-2 in cortical neurons (a1–2) Cortical neurons in stage 3 in their development show distinct axon formation, which can be detected by co staining of MAP-2 and TAU-5. (b1–2) TAU-5 staining and orientation vector used in our study points towards axonal development in later stage within $\sim 180^\circ$. (c1–2) Fluorescent intensity plots demonstrate intracellular polarity of MAP-2 and TAU-5 staining. FMNPs were present but no magnetic field. Neurons polarized randomly.

Here, we generated polar plots summarizing orientation vectors of cells grouped based on one orientation of MEs and two different field strength conditions (Figure S8). The polar plot indicates an impact of the orientation of gradient deformation and an impact of the gradient field strength. The impact of gradient field strength modulated the orientation vector.

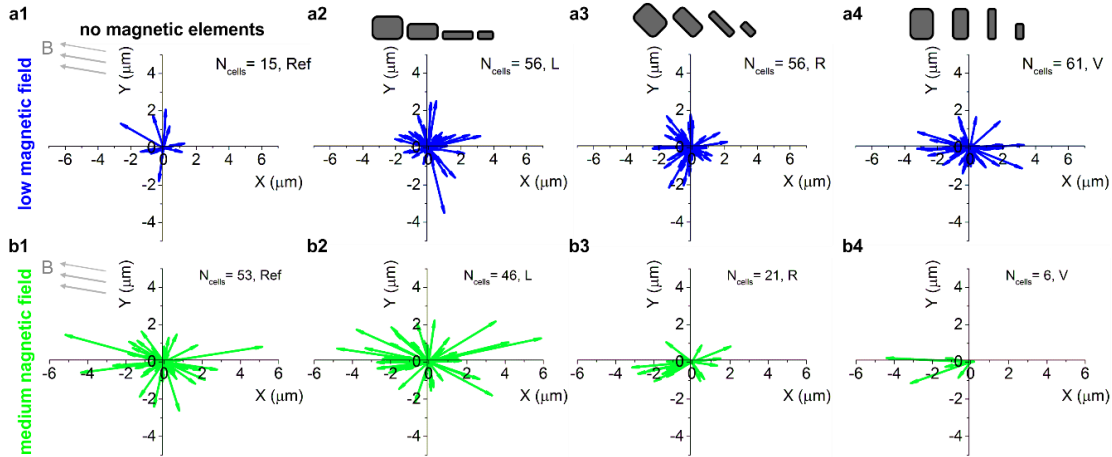


Figure S8: Orientation of magnetic elements impacts direction of neuronal cell polarization. (a1–b4) Polar plots show orientation vectors for cells under permanent magnetic fields and (a1, b1) no magnetic gradient = Ref, (a2, b2) 0° = L(length), (a3, b3) 45° = R(rotated) and (a4, b4) 90° = V(vertical) angled ME orientation with different deformed magnetic field gradients relative to the magnetic field orientation B(x,y,z). (a1, b1) Without magnetic field gradients superparamagnetic fMNP apply no directive forces on neurons, thus neurons polarize along PLL micropatterned ratchet cues. (a2, b2–a4, b4). The orientation of ME impacts the strength of gradient deformation leading to different magnetic forces and gradient slopes. From (a2, b2) length to (a4, b4) vertical oriented ME force and gradient increase, however the gradient increases more than the force. (a2–a4) Within low magnetic fields, fMNP mediated gradients impact the pointing direction (angle) of the vector, but not the length of the orientation vector. (b2–b4) Medium magnetic fields increased the vector length in addition to the pointing direction due to the higher applied external field.

Although local cell adherence to PLL pattern was controlled, we cannot account for the exact position of single cells on the pattern before applying the permanent magnet. We therefore extracted for each single cell their cell location within its reference pattern, which is the pattern code (Figure S9). The pattern code one indicates that the cell adhered on a pattern with one arrow, while six indicates that the cell adhered on a pattern with six arrows in a row. Independent on the magnetic field strength, more cells were evaluated from ratchet patterns with a larger number of arrows (4–6) than fewer number of arrows (1–2), as neurons preferentially adhered to larger patterns. However, this turned out favorably for data analysis, because neurons on larger pattern are exposed to higher pattern forces, thus any unbalanced directionality in polarization towards the MEs are an indicator of force mediated cell polarization. The cell location code indicates the actual position of the cell on its pattern. Again, the number one indicates that the cell sits next to the MEs and six that the cell is the most far away from MEs. Without force (nME) we assume a random cell distribution on the pattern. Comparing cell positions between no force (nME) and force (wME) condition, a shift in cell position within the pattern towards the magnetic elements is observed when force is applied (nME, Figure S9 a1, wME, Figure S9 a2). We concluded that cell displacement must have been taken place with the single cells. For the different magnetic fields $n = 321$ (low), $n = 194$ (medium) and $n = 113$ (strong) single cells were evaluated.

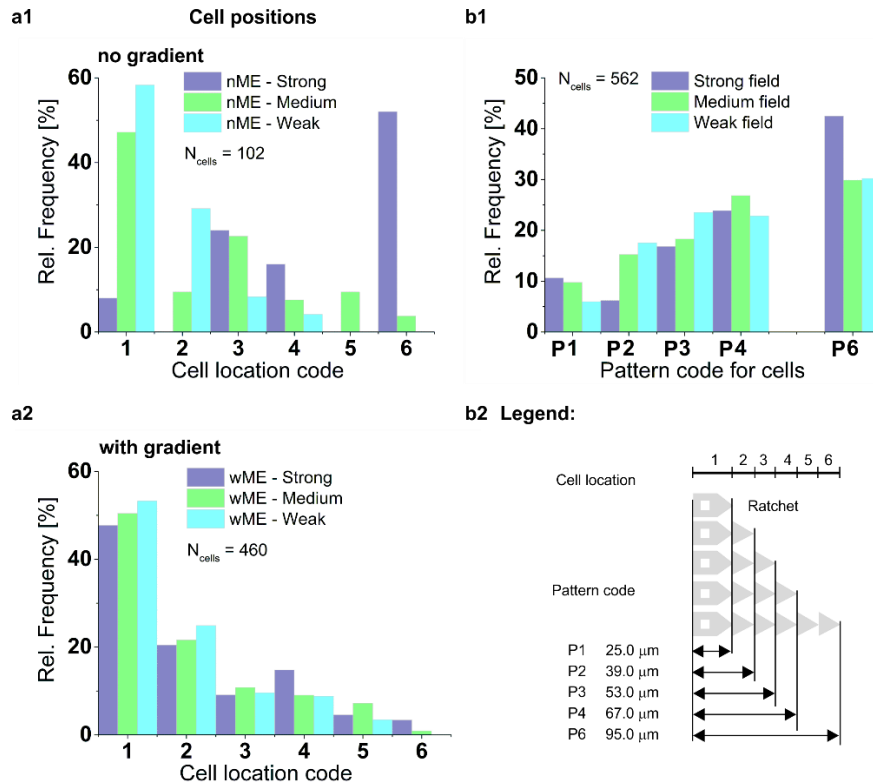


Figure S9: Data distribution for our single cell results. Each cell received two location numbers: one for its cell location and one for its reference pattern. The cell location code describes the position within the ratchet pattern. The pattern code is a number for its reference pattern. A cell sitting on P4 can have a cell location code from 1–4. (a1–2) Extracted cell locations within all evaluated patterns in the presents of different magnetic field strengths (a1) without magnetic gradients (nMEs) and (a2) with magnetic gradients (wME). (b1) Overview of all extracted reference pattern codes for our single cell data. (b2) Legend shows the ratchet design and used nomenclature for our cell location and pattern code.

5. Force Sensitivity within Cell Population.

Figure S10 shows neuronal marker distribution above different PLL pattern widths in support of cell neighbor dependent tau protein orientation on smaller pattern widths with smaller number of cell neighbors ($\leq 50 \mu\text{m}$). All fluorescent intensity signals were extracted, averaged and normalized above the same corresponding width and came from medium magnetic fields with gradients generated through a $12 \mu\text{m} \times 16 \mu\text{m}$, 90° oriented ME.

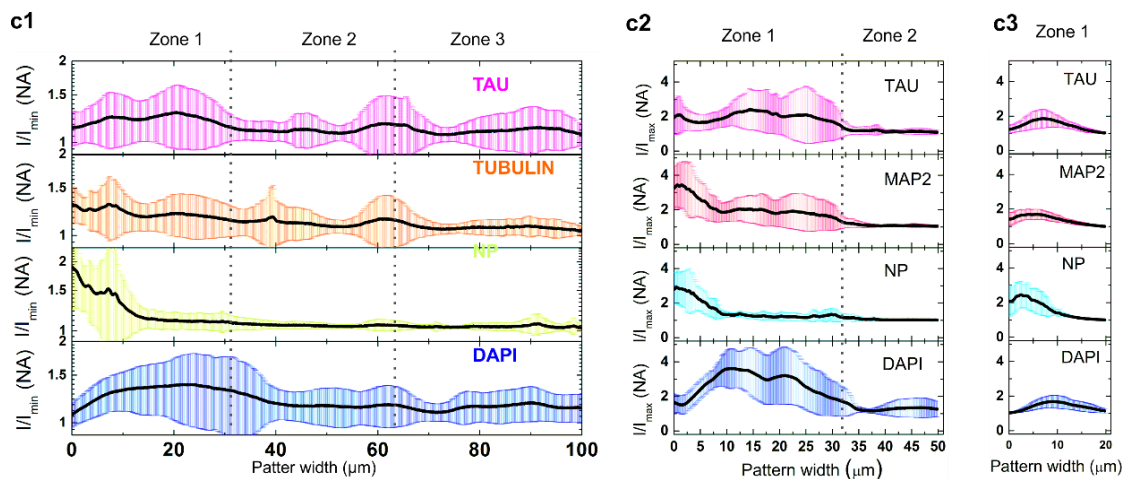


Figure S10: Neuronal marker distribution across different PLL pattern widths. (c1) 100 μm , $N_{\text{ROI}} = 16$, (c2) 50 μm , $N_{\text{ROI}} = 3$ and (c3) 20 μm , $N_{\text{ROI}} = 7$.

Figure S11 provides additional data to evaluate a force threshold for cell displacement and tau orientation (medium magnetic field). The higher the magnetic force, the more tau gets distributed towards the left, where the ME is situated. Also, DAPI signal shifts towards the MEs.

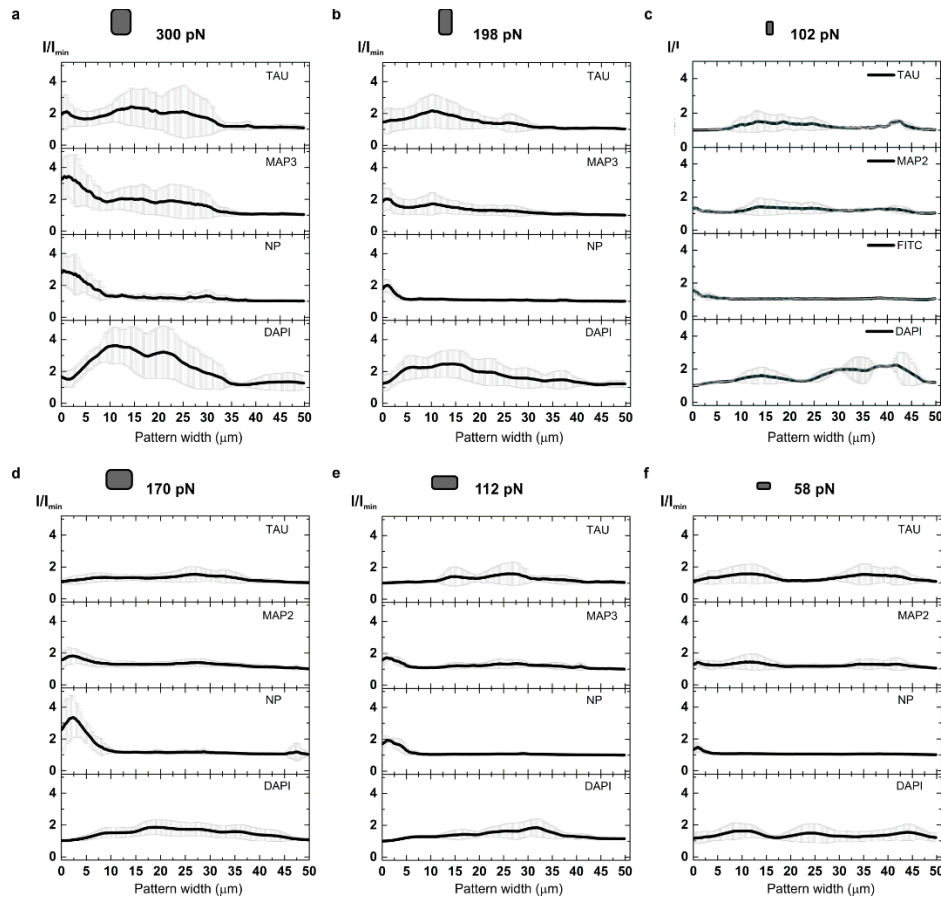


Figure S11: Force induced tau activation and DAPI displacement towards MEs in correlation to different forces. (a – c) height oriented ME sizes: $12 \mu m \times 16 \mu m$ $N_{ROI} = 3$, $8 \mu m \times 16 \mu m$ $N_{ROI} = 5$, $4 \mu m \times 8 \mu m$ $N_{ROI} = 2$, (d – f) length oriented ME sizes: $12 \mu m \times 16 \mu m$, $N_{ROI} = 13$, $8 \mu m \times 16 \mu m$, $N_{ROI} = 5$, $4 \mu m \times 8 \mu m$, $N_{ROI} = 6$.

To exclude an extracellular patterning effect interfering with an intracellular force effect of the fMNPs on the neurons and their network, we performed a control experiment, where fMNPs were patterned next to the MEs before the cells had time to settle down during seeding. Nanoparticle loaded medium was applied to the chip and the chip was placed on top of our magnets for 15 min. The magnetic field gradient locally trapped the free floating fMNPs next to the MEs. After, we seeded our neurons by shortly removing the chip from the magnet, loading the cells and placing the chip back on top of the magnet. The magnetic field was applied for 24 h in the incubator in total. Figure S12 shows a representative image of neurons cultured on the neuromagnetic chip and which were fluorescently labeled with calcein blue after 2 days *in Vitro*. The green signal shows the trapped fMNPs next to MEs. We observed random cell adherence and neurite outgrowth on the neuromagnetic chip, which supports our assumption that the migration and tau reorientation effect in our force study is due to intracellular applied forces by the fMNPs.

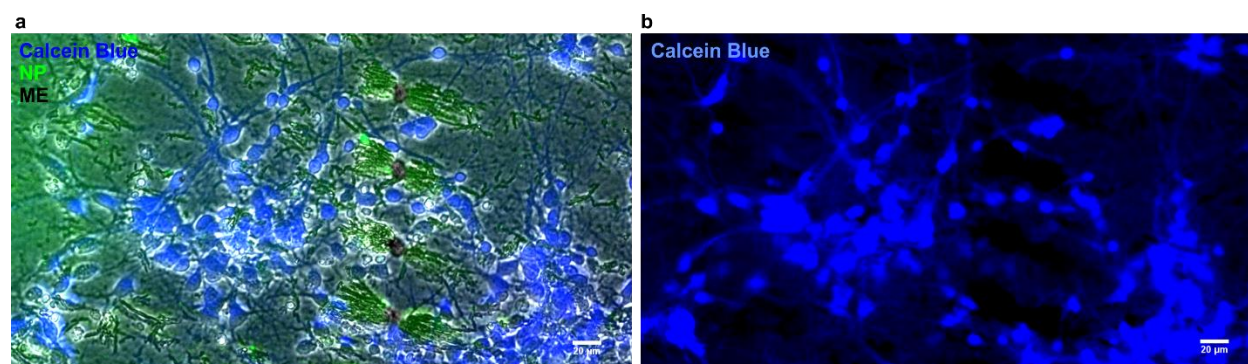


Figure S12: Live cell image of dissociated neurons cultured on the neuromagnetic chip after trapping fMNP next to the MEs. (a) Merged fluorescent and phase contrast image shows $4\ \mu\text{m} \times 8\ \mu\text{m}$ sized MEs and trapped green fMNPs. Neurons were seeded on top of the fMNP pattern and fluorescently labeled with calcein blue after 2 days in culture. (b) The fluorescent image shows only the neurons and their outgrown neurites, which reveal a random growth pattern, mostly independent on the nanoparticle location.

6. Additional Video Files.

V1: 3D Laser confocal z-scan shows fMNPs co-localized with neuronal cytoskeletal markers: TAU-5 and BETA-TUBULIN-III shows spherically shaped, up-taken fMNP clusters in cortical neurons.

7. References.

1. Hatch, G. P.; Stelter, R. E. Magnetic Design Considerations for Devices and Particles used for Biological High-Gradient Magnetic Separation (HGMS) Systems. *J. Magn. Magn. Mater.* **2001**, 225, 262-276.
2. Spedden, E.; White, James D.; Naumova, Elena N.; Kaplan, David L.; Staii, C. Elasticity Maps of Living Neurons Measured by Combined Fluorescence and Atomic Force Microscopy. *Biophys. J.* **2012**, 103, 868–877.
3. Blaire, G.; Masse, A.; Zanini, L.; Gaude, V.; Delshadi, S.; Honegger, T.; Peyrade, D.; Weidenhaupt, M.; Dumas-Bouchiat, F.; Bruckert, F., *et al.* Hybrid Bio-Mag-MEMs Combining Magnetophoresis and Dielectrophoresis. *Eur. Phys. J. B* **2013**, 86, 1–6.

4. Shevkoplyas, S. S.; Siegel, A. C.; Westervelt, R. M.; Prentiss, M. G.; Whitesides, G. M. The Force Acting on a Superparamagnetic Bead Due to an Applied Magnetic Field. *Lab Chip* **2007**, *7*, 1294–1302.
5. Meijering, E.; Dzyubachyk, O.; Smal, I. Methods for Cell and Particle Tracking. In *Methods in Enzymology*, Academic Press: 2012; Vol. 504, pp 183–200.
6. Schaeffer, E.; Norrelykke, S. F.; Howard, J. Surface Forces and Drag Coefficients of Microspheres near a Plane Surface Measured with Optical Tweezers. *Langmuir* **2007**, *23*, 3654–3665.
7. Lipfert, J.; Hao, X.; Dekker, N. H. Quantitative Modeling and Optimization of Magnetic Tweezers. *Biophys. J.* **2009**, *96*, 5040–5049.
8. Steketee, M. B.; Moysidis, S. N.; Jin, X.-L.; Weinstein, J. E.; Pita-Thomas, W.; Raju, H. B.; Iqbal, S.; Goldberg, J. L. Nanoparticle-Mediated Signaling Endosome Localization Regulates Growth Cone Motility and Neurite Growth. *Proc. Natl. Acad. Sci. U.S.A.* **2011**, *108*, 19042–19047.
9. Fass, J. N.; Odde, D. J. Tensile Force-Dependent Neurite Elicitation via Anti-Beta1 Integrin Antibody-Coated Magnetic Beads. *Biophys. J.* **2003**, *85*, 623–636.
10. Tseng, P.; Judy, J. W.; Di Carlo, D. Magnetic Nanoparticle-Mediated Massively Parallel Mechanical Modulation of Single-Cell Behavior. *Nat. Methods* **2012**, *9*, 1113–1119.
11. Pai, J.-H.; Wang, Y.; Salazar, G. T. A.; Sims, C. E.; Bachman, M.; Li, G. P.; Allbritton, N. L. Photoresist with Low Fluorescence for Bioanalytical Applications. *Anal. Chem.* **2007**, *79*, 8774–8780.
12. Scott, M. A.; Wissner-Gross, Z. D.; Yanik, M. F. Ultra-Rapid Laser Protein Micropatterning: Screening for Directed Polarization of Single Neurons. *Lab Chip* **2012**, *12*, 2265–2276.
13. Mahmud, G.; Campbell, C. J.; Bishop, K. J. M.; Komarova, Y. A.; Chaga, O.; Soh, S.; Huda, S.; Kandere-Grzybowska, K.; Grzybowski, B. A. Directing Cell Motions on Micropatterned Ratchets. *Nat. Phys.* **2009**, *5*, 606–612.
14. Cheng, Q.; Komvopoulos, K.; Li, S. Surface Chemical Patterning for Long-Term Single-Cell Culture. *J. Biomed. Mater. Res., Part A* **2011**, *96A*, 507–512.
15. Yang, Y.; Bai, M.; Klug, W. S.; Levine, A. J.; Valentine, M. T. Microrheology of highly crosslinked microtubule networks is dominated by force-induced crosslinker unbinding. *Soft Matter* **2013**, *9*, 383–393.
16. Pinkernelle, J.; Calatayud, P.; Goya, G.; Fansa, H.; Keilhoff, G. Magnetic Nanoparticles in Primary Neural Cell Cultures are Mainly Taken up by Microglia. *BMC Neurosci.* **2012**, *13*, 32–42.
17. dos Santos, T.; Varela, J.; Lynch, I.; Salvati, A.; Dawson, K. A. Quantitative Assessment of the Comparative Nanoparticle-Uptake Efficiency of a Range of Cell Lines. *Small* **2011**, *7*, 3341–3349.
18. Yue, Z.-G.; Wei, W.; Lv, P.-P.; Yue, H.; Wang, L.-Y.; Su, Z.-G.; Ma, G.-H. Surface Charge Affects Cellular Uptake and Intracellular Trafficking of Chitosan-Based Nanoparticles. *Biomacromolecules* **2011**, *12*, 2440–2446.